# Dissociative Photodetachment Studies of $I_2^-$·Ar: Coincident Imaging of Two- and Three-Body Product Channels†

**Kathryn E. Kautzman, Paul E. Crider, David E. Szpunar,‡ and Daniel M. Neumark***

*Department of Chemistry, University of California, Berkeley, California 94720, and Chemical Sciences Division, Lawrence Berkeley National Laboratory, Berkeley, California 94720*

*Received: August 14, 2007; In Final Form: September 25, 2007*

Van der Waals clusters serve as prototypical systems for studying processes of energy transfer. The $I_2$·Ar system has attracted particular interest due to the wide array of decay processes occurring in competition with one another. Here, we present systematic dissociative photodetachment (DPD) studies of the $I_2^-$ and $I_2^-$·Ar anions in the region 4.24−4.78 eV. The resulting neutral fragments are detected by time- and position-sensitive (TPS) coincident imaging. Photofragment mass distributions and translational energy distributions from the DPD of $I_2^-$ are presented and facilitate understanding of the $I_2$·Ar system. For the $I_2$·Ar complex, channels resulting from two-body dissociation leading to $I_2$ + Ar photoproducts are observed at all photon energies employed. We also report the first direct observation of the previously inferred three-body dissociation channel leading to I + I + Ar photoproducts. The relative intensities of each decay channel are investigated in relation to the electronic state being accessed. Translational energy distributions of the $I_2$·Ar complex lend further insight into the decay mechanism for each channel.

## Introduction

Small van der Waals (vdW) clusters are important model systems for understanding the nature of the weak interatomic and intermolecular forces that play a key role in chemical dynamics and spectroscopy.[1] The $I_2$·Ar complex has been a particularly important system of this type,[2] owing in part to the rich variety of dynamical processes that occur upon excitation of the $I_2$ chromophore to the $B^3\Pi_u(0_u^+)$ state, a bound state that correlates to $I + I^*(^2P_{1/2})$ products. The complex is now understood to exist in nearly isoenergetic T-shaped and linear forms, showing discrete and continuum absorption,[3−6] respectively, upon excitation of the $B(^3\Pi 0_u^+)$ state. Mechanisms invoked to explain the decay of the electronically excited complex include vibrational predissociation (VP)[7−11]

$$\mathrm{Ar{\cdot}I_2(B,}\ \nu') \rightarrow \mathrm{Ar} + \mathrm{I_2^*}(\nu \leq \nu') \qquad (1)$$

and electronic predissociation (EP)[8,12,13]

$$\mathrm{Ar{\cdot}I_2(B,}\ \nu') \rightarrow \mathrm{Ar} + \mathrm{I}(^2P_{3/2}) + \mathrm{I}(^2P_{3/2}) \qquad (2)$$

In addition, "one-atom caging"[3,9,14−17] (i.e., emission from intact $I_2$ after excitation above the B state dissociation limit) has been observed and is now attributed to excitation of the linear isomer. VP is the best understood and most experimentally accessible of these processes since the $I_2^*$ product fluoresces and is thus easily detected. In contrast, EP is a dark channel whose existence has been indirectly inferred. Motivated by the possibility of directly observing EP, we have undertaken a complementary approach to previous studies, using dissociative photodetachment (DPD) of $I_2^-$·Ar, which is known to be T-shaped,[18−20] to access the electronic states leading to the dissociation of $I_2$·Ar.

Much of the experimental and theoretical interest in $I_2$·Ar is driven by the observation that the intensity of the VP channel oscillates with $I_2$ (B) vibrational excitation.[7,8,12,13] Two explanations for the origins of these oscillations have been proposed.[6,8] One of these is based on the notion that the VP yield is driven by the nature of the intramolecular vibrational relaxation (IVR) process that transfers vibrational energy from the initially excited $I_2(B, \nu')$ into lower frequency $I_2$·Ar vdW modes until the weak bond breaks.[11] Irregularities in the VP yield result from the sparse manifold of dark states that mediate this process. The other mechanism is based on the competition between VP and EP as a function of $\nu'$; the products from EP do not fluoresce, and if the EP yield oscillates with $\nu'$, the fluorescence from VP will be modulated correspondingly. This latter mechanism is strongly supported by the fluorescence quantum yield measurements of Burke and Klemperer.[12] However, the exact mechanism of EP is still under investigation,[2,21,22] and it has in fact never been directly observed from the excitation of $I_2$·Ar. Detection schemes capable of simultaneously analyzing both two-body and multibody decay events[20,23] permit further investigation of these competitive dissociation channels, as is demonstrated here.

In this work, $I_2$ and $I_2$·Ar are formed through photodetachment of the corresponding anions. We examine the DPD of $I_2^-$ and then compare these results with the dissociative photodetachment of $I_2^-$·Ar. DPD creates $I_2$ and $I_2$·Ar in excited electronic states, which then go on to dissociate by the following schemes:

$$\mathrm{I_2^-} + h\nu \rightarrow \mathrm{I_2^*} + \mathrm{e^-} \rightarrow \mathrm{I} + \mathrm{I} + \mathrm{e^-} \qquad (3)$$

$$\mathrm{I_2^-{\cdot}Ar} + h\nu \rightarrow \mathrm{I_2^*{\cdot}Ar} + \mathrm{e^-} \rightarrow \mathrm{I_2} + \mathrm{Ar} + \mathrm{e^-} \rightarrow \mathrm{I} + \mathrm{I} + \mathrm{Ar} + \mathrm{e^-} \qquad (4)$$

The relevant potential energy curves for $I_2^-$ and $I_2$ in the internuclear distance range of interest are shown in Figure 1.

† Part of the "Giacinto Scoles Festschrift".

* Corresponding author. E-mail: dneumark@berkeley.edu.

‡ Present address: Department of Biological, Chemical, and Physical Sciences, Roosevelt University, Chicago, IL 60605.

10.1021/jp0765401 CCC: $37.00 
Published on Web 11/21/2007

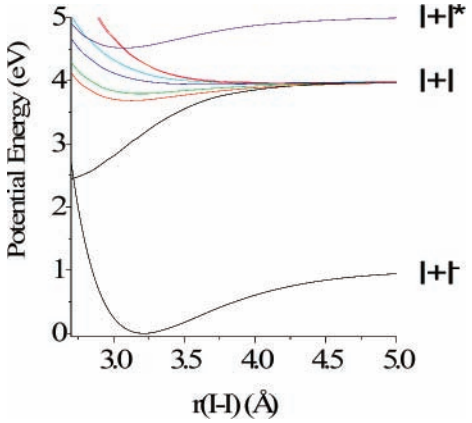


**Figure 1.** $I_2$ anion ground state and low-lying $I_2$ neutral potential energy curves. The anion ground state appears as the lower solid black line. The $^1\Sigma_g^+(0_g^+)$ ground state of the neutral is the higher-lying black line. The bound $A'^3\Pi_u(2_u)$ and $A^3\Pi_u(1_u)$ states appear as solid red and green lines, respectively, while the unbound $B'^3\Pi_u(0_u^-)$ and $B''^1\Pi_u(1_u)$ curves are dark and light blue, respectively. The repulsive $^3\Pi_g1(2_g)$ state appears as a solid magenta line, while the close-lying repulsive $^3\Pi_g(1_g)$ state is orange. The $B^3\Pi_u(0_u^+)$ state appears as the dark purple curve leading to the I + I* products.

The neutral repulsive curves and neutral ground state are from the work of de Jong et al.[24] The $B^3\Pi_u(0_u^+)$ state potential was constructed using a Morse potential with literature values for the well depth and equilibrium internuclear distance.[25] The neutral curves have also been extensively studied by Teichteil and Pelissier.[26] The potential energy curve for the $I_2^-$ $X^2\Sigma_u^+$ ground state was obtained through a combination of femtosecond stimulated emission pumping (fs-SEP) and photoelectron spectroscopy (FPES).[27−29] This curve has a minimum at $R_e$ = 3.205 Å, which locates the center of the Franck−Condon (FC) region accessed by photodetachment.

Figure 2a shows a magnified view of relevant neutral curves near $R_e(I_2^-)$. Photodetachment transitions to these curves were recently mapped out by Parsons et al.[30] via photoelectron spectroscopy of $I_2^-$ at 5.83 eV; Figure 2b shows the portion of the photoelectron spectrum relevant to the work discussed here. The photoelectron spectrum of $I_2^-$·Ar was recorded by Asmis et al.[31] at a photon energy of 4.657 eV (266 nm) and compared with previous spectra of bare $I_2^-$. From the shift in the spectrum induced by the Ar (24 meV) and the binding energy of T-shaped $I_2$·Ar, 29 meV,[11] the dissociation energy of the anion complex was found to be 53 meV. Other than this shift, the photoelectron spectra for bare and complexed $I_2^-$ were very similar, as expected since the Ar only weakly perturbs the anion and neutral. In particular, vertical detachment energies to the excited states of $I_2^-$·Ar were all simply shifted relative to those of $I_2$ by the value of the solvent shift. The other notable difference was that the $I_2^-$·Ar complexes were vibrationally cooler than the bare anions, as evidenced by the reduced contribution from hot bands in the $I_2^-$·Ar spectrum because complexes formed with vibrational energy exceeding the binding energy dissociate prior to mass selection.

In the work described here, a multiparticle time- and position-sensing detector was used to analyze two- and three-body decay channels from the DPD of $I_2^-$ and $I_2^-$·Ar. These data were obtained at a series of photon energies, indicated in Figure 2, enabling us to map out the dynamics as progressively more $I_2$ excited states, up to and including the $B^3\Pi_u(0_u^+)$ state, are accessed. For the $I_2$ system, a large increase in photofragment yield is observed as the photon energy is increased. The translational energy distributions indicate direct dissociation from repulsive potential energy surfaces for all but the highest photon energy. Similar trends are observed with the $I_2$·Ar system. Mass distributions indicate that DPD to $I_2$ + Ar and I + I + Ar occurs at all photon energies used. The I + I + Ar channel grows in accordance with the increased photofragment yield of $I_2$. Translational energy distributions for the three-body dissociation channel are similar to the $I_2$ distributions, indicating direct dissociation at all but the highest photon energy. Two-body decay events (i.e., $I_2$ + Ar) show that little energy is deposited into translation of the photofragments and that these distributions change little with increasing photon energy, consistent with a VP mechanism in which the vibrational energy is channeled into the vdW modes until the weak bond breaks.

## Experimental Procedures

The experimental apparatus shown in Figure 3 has been described in detail previously and will only be briefly described here.[20,32,33] A vibrationally and rotationally cooled beam of $I_2^-$ or $I_2^-$·Ar was created by flowing Ar (25 psig) over $I_2$ crystals at room temperature and expanding the resulting mixture through a pulsed piezoelectric valve operating at 60 Hz. The beam was subsequently crossed by a 1 keV electron beam produced from an electron gun. The resulting anions were accelerated to a laboratory beam energy of 6.5 keV and mass selected using a Bakker time-of-flight mass spectrometer.[34,35] $I_2^-$·Ar anions formed utilizing this type of source have been estimated to have a vibrational temperature of ∼70 K.[31] Anions of the desired mass were dissociatively photodetached by the output of an excimer (Lambda Physik LPX 210, 308 nm) pumped dye laser (Lambda Physik Scanmate 2E). The arrival times and position of the recoiling photofragments were then detected in coincidence by a time- and position-sensitive (TPS) detector located 2.15 m downstream from the dissociation region.

Two methods were used to prevent the undissociated parent ion beam from reaching the detector: either a beam block intercepted the undissociated parent beam or a pulsed electric field (∼200 V) deflected parent (and daughter) ions out of the path of the detector. The beam block blocks a greater area of the detector than the deflecting field, discriminating against dissociation events where little energy is partitioned into translation. Results for $I_2$ were collected using the beam block to discriminate against contributions from $I_2^-$ that were detached but not dissociated. Results presented here for the $I_2$·Ar system were collected using the pulsed electric field to detect the low-energy $I_2$ + Ar channel and low-energy I + I + Ar events. While using the pulsed electric field method allows for more efficient detection of low-energy events than obtained when using the beam block, not all low-energy events are detected in this method, perhaps owing to a "dead spot" in the center of the detector. The dead spot is found to be approximately 6 mm across and 3 mm high, which is slightly smaller than the 7 mm × 5 mm beam block. It was found that for the I + I + Ar channel, a minimum translational energy of 30−50 meV is required for the Ar to successfully clear the dead spot.

The TPS detector, based on the design by Zajfman and Amitay,[36] consists of a standard imaging quality 75 mm Z-stack microchannel plate (MCP) assembly coupled to a phosphor screen (Burle Spec. S9739, Rev. 0). A dichroic beam splitter positioned at 45° to the phosphor screen transmits 50% of the phosphorescence to an image intensifier and CCD camera (Dalsa, CA-D6-D512). The remaining emission is reflected to a 4 × 4 PMT anode array (Hamamatsu H 6568-10) that records precise timing information. The beam splitter preferentially reflects bluer light and transmits redder light, in accordance with

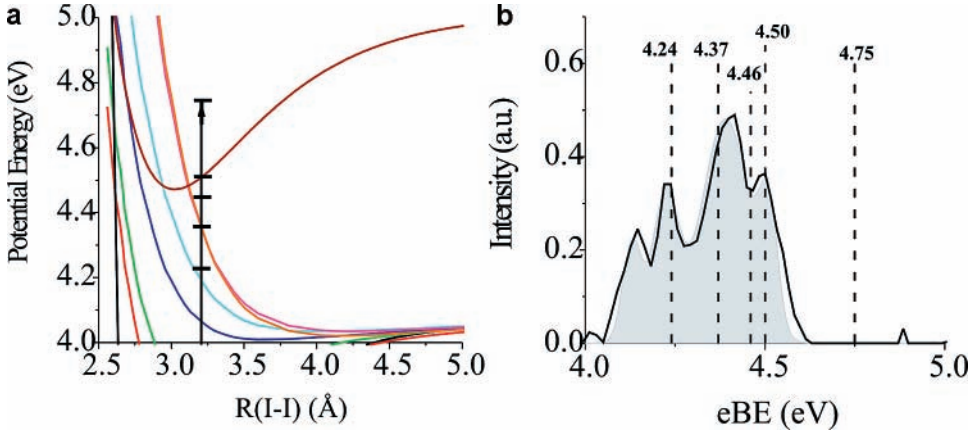


**Figure 2.** (a) Potential energy curves relevant to the current study. (b) Closeup of photoelectron spectrum. The black line is the photoelectron spectrum. The gray fill is the fit to the photoelectron spectrum using the curves from panel a. Vertical dashed lines represent the photon energies used in the current study.

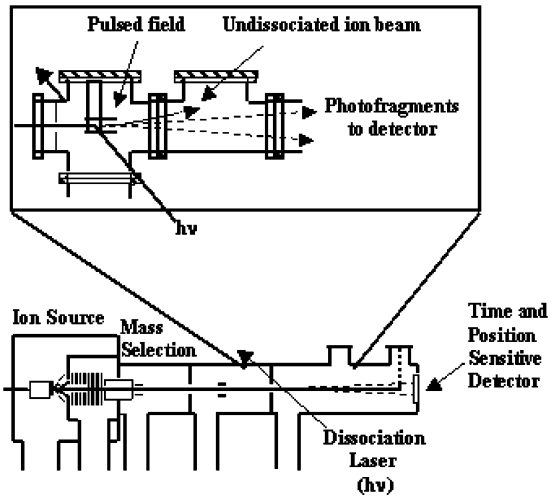


**Figure 3.** Schematic of the fast beam coincident imaging apparatus. Detail of the interaction region showing the pulsed field used to deflect undissociated parent ions from striking the detector is also shown.

the spectral sensitivities of the camera and PMT. This detection scheme permits the detection of both anionic and neutral fragments. Data sets taken with the deflecting field were not found to alter the arrival positions of the photofragments or the center of the dissociation events, indicating that all photofragments are neutral. Additionally, both two- and three-body photofragment events can be detected, enabling the investigation of the two types of dissociation on an approximately equal footing. The coincident time and position information obtained for each event were then used to calculate photofragment mass distributions to determine the products of the dissociation. Translational energy distributions ($P(E_T)$) were also calculated for each product channel. Unlike the triple coincident experiments performed by Hanold et al.,[23] we do not detect the electron and thus do not measure the correlation between the electron kinetic energy (eKE) distribution and the $P(E_T)$ distribution.

## Results

**$I_2^-$: Photofragment Yield and Translational Energy Distributions.** To establish a baseline for the role of the solvating Ar, the dissociative photodetachment of $I_2^-$ was investigated at several photon energies between 4.24 and 4.75 eV to determine how the dissociation of $I_2$ changes with increasing photon energy. Photofragment yields and translational energy distributions are displayed in Figure 4. All products were found to be neutral. As shown in Figure 4a, the $I_2$ dissociation yield grew rapidly between 4.37 and 4.50 eV. The individual data sets have been normalized for laser power, number of laser shots, and ion production. Data sets were taken at the same photon energies on different days to determine the fluctuations in dissociation due to day-to-day fluctuations of experimental parameters. Despite normalization, a difference in the absolute intensity of dissociation (up to 40%) is still apparent between data sets taken with the same photon energies due to fluctuations in laser power, laser alignment, and ion production. However, the qualitative trend of increasing dissociation with increasing photon energy far exceeds the fluctuations between data sets taken at the same photon energy.

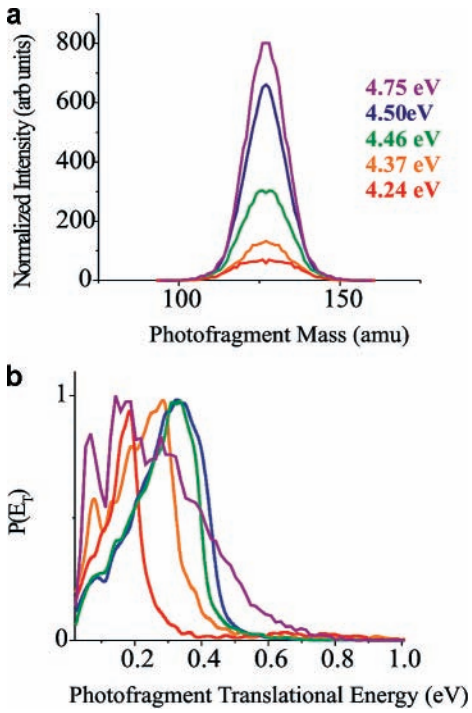


**Figure 4.** (a) Photofragment mass distributions for $I_2^-$ DPD. (b) Translational energy distributions for $I_2^-$ DPD.

The $P(E_T)$ distributions obtained from $I_2^-$ DPD are plotted in Figure 4b. In general, the maximum value of $E_T$ increases with photon energy. Moreover, the distributions are structured, particularly the one at 4.75 eV, which shows three peaks and a tail extending to high energy.

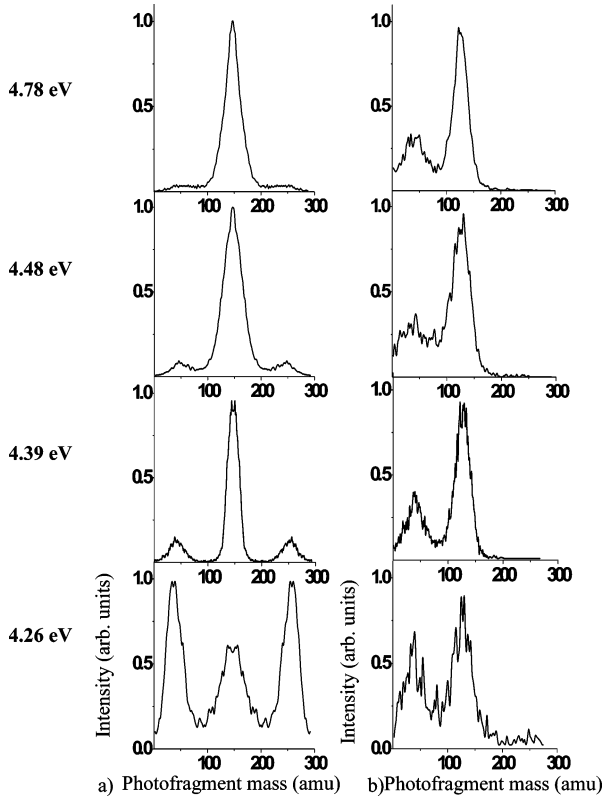


**Figure 5.** Photofragment mass distributions for $I_2^-$·Ar. (a) Photofragment mass distributions for two-body events. (b) Photofragment mass distributions for three-body events.

**$I_2^-$·Ar Mass Distributions and P($E_T$) Distributions.** Figure 5a,b shows the mass distributions corresponding to channels in which two and three fragments, respectively, were detected from the DPD of $I_2^-$·Ar at several photon energies. To facilitate comparison with the DPD of bare $I_2^-$, the photon energies in Figure 5 were increased by 24 meV, the difference between the electron affinities of $I_2$·Ar and bare $I_2$.[31] In Figure 5a, the peaks corresponding to 40 and 254 amu represent dissociation to Ar + $I_2$ products. The central peak corresponds to two equal mass fragments, each with a mass of 147 amu. This channel is assigned to dissociation events producing I + I + Ar products where the two I fragments are detected but the Ar does not possess enough translational energy to clear the dead spot in the center of the detector. Because the third fragment was not detected, our analysis program assigned the channel to a two-body event producing two particles of equal mass (147 amu). Figure 5a shows that the intensity of the central peak rises with increasing photon energy, correlating with the total I + I signal seen from bare $I_2^-$. Figure 5b shows that three-body dissociation events in which all three fragments are directly observed also occur at each photon energy, with a peak at 40 amu and a peak of roughly double the intensity at 127 amu.

Figure 6 shows P($E_T$) distributions for three-body decay events observed at the three highest photon energies, with the $I_2^-$ DPD at the corresponding photon energy shown as a dashed line for comparison. The fraction of three-body events at 4.26 eV was too small to produce a meaningful distribution. Note that events are counted as three-body events only if the Ar atom has sufficient recoil energy to clear the dead spot in the middle of the detector, which means, for example, that three-body events that occur in the plane parallel to the detector are favored, as are higher translational energy events. Distributions calculated from the events where only the I fragments were detected (mass 147 peak in Figure 5) yield distributions peaked at slightly lower

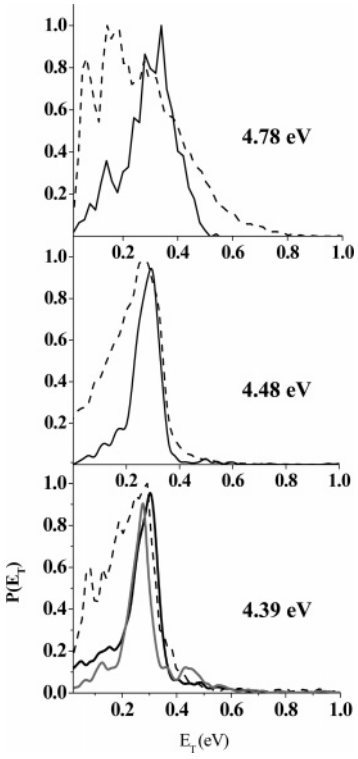


**Figure 6.** Translational energy distributions for the I + I + Ar photoproducts channel. Translational energy distributions for $I_2^-$ are shown as dashed lines. The 4.39 eV panel also displays the translational energy distribution calculated using events where Ar is undetected as a gray line.

translational energies, as shown by the gray line at 4.39 eV in Figure 6. This shift is expected since the contribution to the total recoil energy from the Ar atom is neglected. In any case, comparison of the two types of distributions shows that any bias in the true three-body distributions is small and that the Ar atom contributes relatively little to $E_T$. Comparison to the $I_2^-$ DPD shows that at the two lower photon energies, the distributions match quite well at high $E_T$, but at the highest energy, the tail at high $E_T$ in the bare $I_2^-$ distribution is suppressed in the DPD of $I_2^-$·Ar.

Figure 7 shows the translational energy distributions for two-body decay events of $I_2^-$·Ar. All two-body distributions presented have been normalized with a detector acceptance function (DAF), which accounts for geometric factors that prevent the collection of all of the dissociation events. The details of the DAF have been described previously.[32] The energy partitioned into photofragment translation for the two-body dissociation channel is found to peak near zero for all photon energies. Within the limitations of our data collection and analysis programs, these distributions are found to be the same at all photon energies.

## Discussion

In this section, we first analyze the results for the bare $I_2$ molecule by examining the changes in the photofragment mass distributions as the photon energy increases. The translational energy distributions are then utilized to consider the DPD pathways of $I_2^-$. Using insights gained from the analysis of $I_2^-$, the mass distributions and translational energy distributions from DPD of $I_2^-$·Ar are then examined.

**$I_2^-$ Photofragment Yield.** By examining the photoelectron spectrum and relativistic potentials provided by de Jong et al. (see Figure 2), it can be determined that at a photon energy of

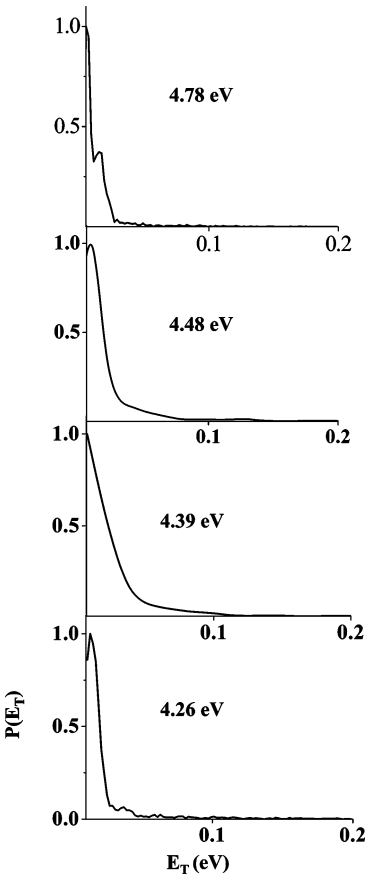


**Figure 7.** Translational energy distributions for the $I_2$ + Ar photoproducts channel.

4.24 eV, we are accessing the bound X, A′, and A states of $I_2$, with slight contributions from the unbound B′ and B″ states. At higher photon energies (4.37, 4.46, and 4.50 eV), as more of the repulsive translational states supported by the $^3\Pi$ curves become accessible, the dissociation yield rises sharply. Contributions from the B state, which is known to undergo predissociation,[37−40] are only observed at the highest photon energy of 4.75 eV. The increase in photofragment yield between 4.50 and 4.75 eV is slightly greater than the average intensity fluctuations and is consistent with the occurrence of predissociation; further evidence for this process is presented in $I_2^-$ Translational Energy Distributions.

**$I_2^-$·Ar Mass Distributions.** The results for $I_2^-$ provide a framework for the photofragment mass distributions from $I_2^-$·Ar dissociative photodetachment. The key result is that the competition between two- and three-body DPD mirrors the photofragment yield from $I_2^-$. At the lowest photon energy, 4.26 eV, $I_2$ + Ar production appears to dominate, but the contribution from three-body decay increases significantly as the photon energy is raised. The two-body channel presumably results from VP from Ar complexed to vibrationally excited $I_2$ in its bound X, A′, and A states. As the photon energy is raised to 4.48 eV, three-body dissociation increases, owing to the progressively greater contribution from directly repulsive states of $I_2$. At the highest energy, 4.78 eV, where the excited Ar·$I_2$(B) complex is accessible, both channels are accessible via VP and EP. There appears to be relatively more three-body dissociation at 4.78 eV than at 4.48 eV, again mirroring the results for bare $I_2^-$ and possibly reflecting the contribution from EP.

**$I_2^-$ Translational Energy Distributions.** We now examine the P($E_T$) distributions for the dissociative photodetachment of $I_2^-$. The general trend seen in Figure 4 is that as the photon energy increases, the P($E_T$) distributions shift toward higher translational energy. This trend can arise from several effects. With increasing photon energy, transitions to higher lying repulsive states become accessible (see Figure 2a), resulting in a larger translational energy release since all the repulsive states accessed in this experiment correlate to the same asymptote. Moreover, for dissociative detachment to a particular repulsive electronic state, higher translational energy levels of that state are accessed with increasing photon energy until the entire FC range of levels is covered. These points are clarified by superimposing the photon energies used onto the fit for the $I_2^-$ photoelectron spectrum, as shown in Figure 2b.

Thus, at 4.24 eV, the entire FC profile of the $B'^3\Pi_u(0_u^-)$ state and most of the profile of the $B''^1\Pi_u(1_u)$ state can be reached. The photon energies 4.37, 4.46, and 4.5 eV additionally access part, nearly all, and all of the translational energy levels, respectively, associated with the close-lying $^3\Pi_g(2_g)$ and $a^3\Pi_g(1_g)$ states. Hence, the faster distribution at 4.37 eV relative to 4.24 eV results primarily from accessing higher electronic states, whereas the progressively faster distributions at 4.46 and 4.50 eV as compared to 4.37 eV result from higher-lying translational energy levels associated with the same electronic states. At 4.50 eV, lower vibrational levels of the $B^3\Pi_u(0_u^+)$ state are also available as shown by the photoelectron spectrum, but this is a bound rather than repulsive state. Finally, at 4.75 eV, all translational and vibrational levels of the electronic states listed previously are accessible, and it is of interest to compare the resulting P($E_T$) distribution directly to the photoelectron spectrum of $I_2^-$ as discussed next.

In dissociative photodetachment, the energy available to be partitioned into translation corresponds to

$$E_T = h\nu + E_{int}^- - E_{int} - D_0 - \mathrm{EA(I)} - \mathrm{eKE} \qquad (5)$$

where $E_T$ is the translational energy of the photofragments, $h\nu$ is the photon energy, and $E_{int}$ and $E_{int}^-$ are the internal energy of the products and parent anion beam, respectively. Since the product of $I_2$ dissociation produces atoms, and the channel to produce I* is not energetically accessible, $E_{int}$ is zero. $E_{int}^-$ is also assumed to be negligible for these studies. $D_0$ is the dissociation energy of $I_2^-$, EA is the electron affinity of I, and eKE is the kinetic energy of the departing electron. Inserting the known values for $D_0$, 1.007 eV,[41] and EA(I), 3.059 eV,[42] reduces eq 5 to

$$E_T = h\nu - 4.066 - \mathrm{eKE} \qquad (6)$$

In any non-resonant photodetachment process, the photoelectron kinetic energy distribution represents, to first-order, a FC mapping of the initial anion wavefunction onto the energetically accessible neutral electronic states, regardless of whether they are bound or repulsive states. For a purely repulsive state of a diatomic, the photoelectron spectrum is necessarily unstructured, and if several repulsive states are accessed, the photoelectron spectrum will be comprised of a series of broad peaks, each corresponding to a different repulsive neutral state. According to eq 6, there is a one-to-one correspondence between eKE and $E_T$, and the P($E_T$) distribution should resemble the photoelectron (PE) spectrum.

In Figure 8, the $I_2^-$ PE spectrum[30] has been overlaid with the P($E_T$) distribution at 4.75 eV, with the energy scale shifted according to eq 6. While the PE spectrum shows four peaks, the P($E_T$) distribution shows only three, with a tail extending to high energy instead of the fourth peak. This observation reflects the fact that the B state is bound, so that eqs 5 and 6 no

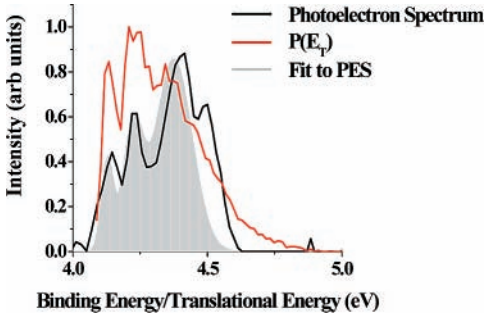


**Figure 8.** Comparison between the photoelectron spectrum and the translational energy distribution taken at 4.78 eV. The contributions from the *B* state have been removed from the gray fit to the photoelectron spectrum.

longer apply. Thus, instead of seeing a corresponding peak in the P($E_T$) distribution reflecting FC overlap with the neutral translational wavefunctions, any signal from the B state must arise from its predissociation via repulsive curves that correlate to ground state I + I products. It appears that this process is the origin of the high-energy tail in the P($E_T$) distribution.

Examination of the remaining features shows that the first two peaks, corresponding to the repulsive B′ and B″ states, line up well in the P($E_T$) distribution and PE spectrum. The third peak, from the repulsive $^3\Pi_g(2_g)$ and $a^3\Pi_g(1_g)$ states, appears in both but is shifted toward slightly higher energy in the PE spectrum. This shift is largely due to the contribution of the B state to the PE spectrum, as can be seen by the significantly smaller shift between the third peaks of the P($E_T$) distribution and the gray fill in Figure 8, which represents the original fit to the PE spectrum (shown in Figure 2) with the B state contribution removed.

**$I_2^-$·Ar Translational Energy Distributions. $I_2$ + Ar Channel.** The energy partitioned into photofragment translation for the two-body $I_2$ + Ar dissociation channel peaks near zero for all photon energies as shown in Figure 7. Photodetachment creates highly excited $I_2$ in various bound electronic states that can eject the Ar by vibrational predissociation (VP). Vibrational quanta are transferred from the $I_2$ chromophore to the weak vdW bond until this bond breaks. At a photon energy of 4.26 eV, the X, A′, and A states can be formed with enough vibrational energy to undergo VP. The vibrational frequencies of these states are 21 meV for the X state and 11 meV for both A′ and A states, while the binding energy of the Ar for the neutral complex is ~30 meV.[41] No other bound states become available until the B state is accessed. For the photon energies used in this work, significant population of the B state occurs at 4.78 eV. As a result, all contributions from VP channels are expected to be open at 4.24 eV, and no changes are expected, if any, until 4.78 eV. In fact, we see no evidence for a change in the P($E_T$) distribution at this energy, which may reflect in part that the contribution from the B state is obscured by VP from the lower-lying bound states of $I_2$. In any case, all the P($E_T$) distributions for $I_2$ + Ar, peaking near zero and showing no dependence on photon energy, suggest that the IVR-mediated VP mechanism proposed for the B state applies to the lower-lying bound states of $I_2$, as well.

**I + I + Ar Channel.** The translational energy distributions for dissociative photodetachment of $I_2^-$·Ar to I + I + Ar can be compared directly to those for I + I from $I_2^-$ in Figure 6 to gauge the effect of the Ar atom on the overall dynamics. Again, we see that the three-body translational energy distributions shift to higher translational energies with increasing photon energies. As with $I_2$, the shift to higher translational energies corresponds to the mapping of the full FC region onto the repulsive curves. It can also be seen that the width of the translational energy distributions for the complex are narrower and tail out to slightly lower translational energies. It is found that the narrower peak of $I_2$·Ar comes from having less intensity at low-energy events. This difference at low energy is from our detection bias toward events in which the Ar atom does not clear the dead spot.

At 4.78 eV, depletion of the high $E_T$ tail for $I_2^-$·Ar as compared to bare $I_2^-$ may reflect the competitive roles of VP and EP. For the $I_2$·Ar complex, the role of VP increases as higher vibrational levels of the B state are accessed. The experiments of Levy et al. showed that fluorescence from the $I_2$·Ar complex is only observed for $\nu > 12$.[7] Since EP is a dark channel, the absence of fluorescence below $\nu = 12$ indicates that EP is the dominant channel. The experiments of Goldstein et al. showed that the efficiencies of EP and VP are competitive in the region of $12 < \nu < 26$.[8] Therefore, it is reasonable to assume that the greater efficiency of VP at higher vibrational levels essentially shuts off the EP channel, thus depleting the signal at highest $E_T$ for three-body dissociation. One might also expect to see a concurrent growth in the mass distributions of the two-body channel, but dissociation from the lower-lying repulsive states may swamp out any small additions from the two-body channel to the overall mass distribution. Furthermore, the two-body channel is significantly more difficult to detect than the three-body channel owing to the fact that less energy is partitioned into translation.

## Conclusion

The experiments presented here have used dissociative photodetachment of $I_2^-$ and $I_2^-$·Ar at several photon energies to access repulsive and predissociating states of $I_2$ with the goal of better understanding the role of two- and three-body decay of the $I_2$·Ar complex. For bare $I_2^-$, the I + I photofragment yield increases dramatically with a photon energy above 4.3 eV, as progressively more directly repulsive electronic states of $I_2$ become accessible. This effect is mirrored in the photofragment yields from DPD of $I_2^-$·Ar, in which the contribution from three-body decay to I + I + Ar versus two-body decay to $I_2$ + Ar rises sharply above 4.26 eV.

The translational energy distributions of the photofragments from both anions are also illuminating. For bare $I_2^-$, the P($E_T$) distribution shifts to higher $E_T$ with increasing photon energy. The most interesting result is at the highest photon energy, 4.75 eV, where one observes peaks from direct dissociation on the repulsive B′, B″, $^3\Pi_g(2_g)$, and $a^3\Pi_g(1_g)$ states of $I_2$, and a tail extending to high $E_T$ assigned to predissociation of the B state. For $I_2^-$·Ar, the origin and dynamics of the $I_2$ + Ar and I + I + Ar channels are very different. The two-body channel, which peaks near $E_T = 0$ for all photon energies used here, is primarily attributed to vibrational predissociation of $I_2$·Ar from vibrationally excited $I_2$ formed in its X, A′, and A states, although some may occur at the highest energy from $I_2$(B). The P($E_T$) distributions for three-body dissociation exhibit similar trends to those seen for bare $I_2^-$, as expected since this channel results from dissociation on the same $I_2$ potential energy curves. We do, however, find that that at the highest photon energy, where the B state of $I_2$ is accessed, the high-energy tail seen for the bare ion is depleted for $I_2^-$·Ar, an effect attributed to the competition between vibrational predissociation and three-body decay.

**Acknowledgment.** This work was supported by the Director, Office of Basic Energy Sciences, Chemical Sciences Division

of the U.S. Department of Energy under Contract DE-AC02-05CH11232. The authors also thank Dr. Bradley F. Parson for useful discussions and for the photoelectron spectrum of $I_2$. K.E.K. also acknowledges support from the Chancellors Predoctoral Opportunity Fellowship from the University of California.

## References and Notes

(1) Rohrbacher, A.; Halberstadt, N.; Janda, K. C. *Annu. Rev. Phys. Chem.* **2000**, *51*, 405.
(2) Buchachenko, A.; Halberstadt, N.; Lepetit, B.; Roncero, O. *Int. Rev. Phys. Chem.* **2003**, *22*, 153.
(3) Miller, A. E. S.; Chuang, C. C.; Fu, H. C.; Higgins, K. J.; Klemperer, W. *J. Chem. Phys.* **1999**, *111*, 7844.
(4) Roncero, O.; Lepetit, B.; Beswick, J. A.; Halberstadt, N.; Buchachenko, A. A. *J. Chem. Phys.* **2001**, *115*, 6961.
(5) Bastida, A.; Zuniga, J.; Requena, A.; Miguel, B.; Beswick, J. A.; Vigue, J.; Halberstadt, N. *J. Chem. Phys.* **2002**, *116*, 1944.
(6) Burke, M. L.; Klemperer, W. *J. Chem. Phys.* **1993**, *98*, 1797.
(7) Johnson, K. E.; Sharfin, W.; Levy, D. H. *J. Chem. Phys.* **1981**, *74*, 163.
(8) Goldstein, N.; Brack, T. L.; Atkinson, G. H. *J. Chem. Phys.* **1986**, *85*, 2684.
(9) Burroughs, A.; Heaven, M. C. *J. Chem. Phys.* **2001**, *114*, 7027.
(10) Roncero, O.; Buchachenko, A. A.; Lepetit, B. *J. Chem. Phys.* **2005**, *122*.
(11) Blazy, J. A.; Dekoven, B. M.; Russell, T. D.; Levy, D. H. *J. Chem. Phys.* **1980**, *72*, 2439.
(12) Burke, M. L.; Klemperer, W. *J. Chem. Phys.* **1993**, *98*, 6642.
(13) Kubiak, G.; Fitch, P. S. H.; Wharton, L.; Levy, D. H. *J. Chem. Phys.* **1978**, *68*, 4477.
(14) Valentini, J. J.; Cross, J. B. *J. Chem. Phys.* **1982**, *77*, 572.
(15) Fei, S. L.; Zheng, X. N.; Heaven, M. C.; Tellinghuisen, J. *J. Chem. Phys.* **1992**, *97*, 6057.
(16) Zamith, S.; Meier, C.; Halberstadt, N.; Beswick, J. A. *J. Chem. Phys.* **1999**, *110*, 960.
(17) Darr, J. P.; Glennon, J. J.; Loomis, R. A. *J. Chem. Phys.* **2005**, *122*.
(18) Batista, V. S.; Coker, D. F. *J. Chem. Phys.* **1999**, *110*, 6583.
(19) Faeder, J.; Parson, R. *J. Chem. Phys.* **1998**, *108*, 3909.
(20) Hoops, A. A.; Gascooke, J. R.; Faulhaber, A. E.; Kautzman, K. E.; Neumark, D. M. *Chem. Phys. Lett.* **2003**, *374*, 235.
(21) Roncero, O.; Halberstadt, N.; Beswick, J. A. *Chem. Phys. Lett.* **1994**, *226*, 82.
(22) Bastida, A.; Zuniga, J.; Requena, A.; Halberstadt, N.; Beswick, J. A. *Chem. Phys.* **1999**, *240*, 229.
(23) Hanold, K. A.; Sherwood, C. R.; Garner, M. C.; Continetti, R. E. *Rev. Sci. Instrum.* **1995**, *66*, 5507.
(24) deJong, W. A.; Visscher, L.; Nieuwpoort, W. C. *J. Chem. Phys.* **1997**, *107*, 9046.
(25) Martin, F.; Bacis, R.; Churassy, S.; Verges, J. *J. Mol. Spectrosc.* **1986**, *116*, 71.
(26) Teichteil, C.; Pelissier, M. *Chem. Phys.* **1994**, *180*, 1.
(27) Davis, A. V.; Wester, R.; Bragg, A. E.; Neumark, D. M. *J. Chem. Phys.* **2003**, *118*, 999.
(28) Zanni, M. T.; Batista, V. S.; Greenblatt, B. J.; Miller, W. H.; Neumark, D. M. *J. Chem. Phys.* **1999**, *110*, 3748.
(29) Zanni, M. T.; Davis, A. V.; Frischkorn, C.; Elhanine, M.; Neumark, D. M. *J. Chem. Phys.* **2000**, *112*, 8847.
(30) Parsons, B. F.; Sheehan, S. M.; Kautzman, K. E.; Yen, T. A.; Neumark, D. M. *J. Chem. Phys.* **2006**, *125*, 244301.
(31) Asmis, K. R.; Taylor, T. R.; Xu, C. S.; Neumark, D. M. *J. Chem. Phys.* **1998**, *109*, 4389.
(32) Cyr, D. R. *Fast Beam Studies of Free Radical Dissociation*, Ph.D. Thesis, University of California, Berkeley: Berkeley, CA, 1993.
(33) Hoops, A. A. *Fast Beam Photodissociation Spectroscopy and Dynamics of Small Molecules*, Ph.D. Thesis, University of California, Berkeley: Berkeley, CA, 2003.
(34) Bakker, J. M. B. *J. Phys. E* **1973**, *6*, 785.
(35) Bakker, J. M. B. *J. Phys. E* **1974**, *7*, 364.
(36) Amitay, Z.; Zajfman, D. *Rev. Sci. Instrum.* **1997**, *68*, 1387.
(37) Busch, G. E.; Mahoney, R. T.; Morse, R. I.; Wilson, K. R. *J. Chem. Phys.* **1969**, *51*, 837.
(38) Kato, H.; Baba, M. *Chem. Rev.* **1995**, *95*, 2311.
(39) Chutjian, A.; James, T. C. *J. Chem. Phys.* **1969**, *51*, 1242.
(40) Chutjian, A.; Link, J. K.; Brewer, L. *J. Chem. Phys.* **1967**, *46*, 2666.
(41) Zanni, M. T.; Taylor, T. R.; Greenblatt, B. J.; Soep, B.; Neumark, D. M. *J. Chem. Phys.* **1997**, *107*, 7613.
(42) Hotop, H.; Lineberger, W. C. *J. Phys. Chem. Ref. Data* **1985**, *14*, 731.